PAPER

Assessment of sequence dependent geometric distortion in contrast-enhanced MR images employed in stereotactic radiosurgery treatment planning

To cite this article: Eleftherios P Pappas *et al* 2018 *Phys. Med. Biol.* **63** 135006

IOP Publishing Phys. Med. Biol. 63 (2018) 135006 (12pp) https://doi.org/10.1088/1361-6560/aac7bf

Physics in Medicine & Biology

IPEM Institute of Physics and Engineering in Medicine

PAPER

RECEIVED
18 March 2018

REVISED
17 May 2018

ACCEPTED FOR PUBLICATION
24 May 2018

PUBLISHED
25 June 2018

Assessment of sequence dependent geometric distortion in contrast-enhanced MR images employed in stereotactic radiosurgery treatment planning

Eleftherios P Pappas[1], Ioannis Seimenis[2], Dimitrios Dellios[1], Georgios Kollias[3], Kostas I Lampropoulos[3] and Pantelis Karaiskos[1,3]

[1] Medical Physics Laboratory, Medical School, National and Kapodistrian University of Athens, 75 Mikras Asias, 115 27 Athens, Greece
[2] Medical Physics Laboratory, Medical School, Democritus University of Thrace, 2nd building of Preclinical Section, University Campus, 68100 Alexandroupolis, Greece
[3] Medical Physics and Gamma Knife Department, Hygeia Hospital, Kifissias Avenue and 4 Erythrou Stavrou, Marousi, 151 23 Athens, Greece

E-mail: pkaraisk@med.uoa.gr

Keywords: MRI, distortion, susceptibility, contrast agent, gadolinium, magnetic field inhomogeneity, stereotactic radiosurgery

Abstract

This work focuses on MR-related sequence dependent geometric distortions, which are associated with B_0 inhomogeneity and patient-induced distortion (susceptibility differences and chemical shift effects), in MR images used in stereotactic radiosurgery (SRS) applications. Emphasis is put on characterizing distortion at target brain areas identified by gadolinium diethylenetriamine pentaacetic acid (Gd-DTPA) paramagnetic contrast agent uptake.

A custom-made phantom for distortion detection was modified to accommodate two small cylindrical inserts, simulating small brain targets. The inserts were filled with Gd-DTPA solutions of various concentrations (0–20 mM). The phantom was scanned at 1.5 T unit using both the reversed read gradient polarity (to determine the overall distortion as reflected by the inserts centroid offset) and the field mapping (to determine B_0 inhomogeneity related distortion in the vicinity of the inserts) techniques. Post-Gd patient images involving a total of 10 brain metastases/targets were also studied using a similar methodology.

For the specific imaging conditions, contrast agent presence was found to evidently affect phantom insert position, with centroid offset extending up to 0.068 mm mM^{-1} (0.208 ppm mM^{-1}). The Gd-DTPA induced distortion in patient images was of the order of 0.5 mm for the MRI protocol used, in agreement with the phantom results. Total localization uncertainty of metastases-targets in patient images ranged from 0.35 mm to 0.87 mm, depending on target location, with an average value of 0.54 mm (2.24 ppm). This relative wide range of target localization uncertainty results from the fact that the B_0 inhomogeneity distortion vector in a specific location may add to or partly counterbalance Gd-DTPA induced distortion, thus increasing or decreasing, respectively, the total sequence dependent distortion.

Although relatively small, the sequence dependent distortion in Gd-DTPA enhanced brain images can be easily taken into account for SRS treatment planning and target definition purposes by carefully inspecting both the forward and reversed polarity series.

1. Introduction

Magnetic Resonance (MR) images exhibit superior soft tissue contrast compared to computed tomography (CT) images and, consequently, are increasingly employed in radiotherapy treatment planning (Schmidt and Payne 2015, Weygand *et al* 2016), either along with CT images or even alone (Johnstone *et al* 2017, Owrangi *et al* 2018). Although the intrinsic MRI contrast is superior and much more versatile to that of CT, target localization and delineation may require the employment of contrast agents that enhance the signal difference between target

and surrounding normal tissue. For instance, paramagnetic extracellular contrast agents, such as the gadolinium diethylenetriamine pentaacetic acid (Gd-DTPA), shorten the T1 relaxation time of brain lesions taking up such agents (McRobbie *et al* 2017). As a result, even tiny brain metastases brighten up in T1-weighted (T1w) images acquired after Gd-DTPA administration, thus facilitating their detection and delineation. This contrast enhancement mechanism is routinely exploited for MRI-based treatment planning in advanced radiotherapy applications (Schmidt and Payne 2015), such as stereotactic radiosurgery (SRS) and stereotactic radiotherapy (SRT), in which target localization accuracy is of high importance (Karaiskos *et al* 2014, Winey and Bussiére 2014, Roper *et al* 2015, Jin *et al* 2016, Pappas *et al* 2017a).

MR images suffer from inherent distortions. Sources of distortion relate to either the MRI system (Doran *et al* 2005, Baldwin *et al* 2007, Moutsatsos *et al* 2013, Tadic *et al* 2014, Pappas *et al* 2016, Gustafsson *et al* 2017, Damyanovich *et al* 2018) or the subject being scanned (Baldwin *et al* 2009, Stanescu *et al* 2012, Wang *et al* 2013, Adjeiwaah *et al* 2018). In the former case, geometric distortions arise from gradient field non-linearity and static magnetic field (B_0) inhomogeneity. MR scanner vendors equip their units with post-imaging correction algorithms which reduce gradient field non-linearity distortions (Wang *et al* 2004, Karger *et al* 2006), since they are fairly predictable (Baldwin *et al* 2007, Damyanovich *et al* 2018). Nevertheless, residual distortions may still be considerable in areas distant from the isocenter (Baldwin *et al* 2007, Pappas *et al* 2016). Residual gradient field non-linearity related distortions can be estimated and corrected with the aid of specially designed phantoms (Weygand *et al* 2016). Patient-induced distortions relate to magnetic susceptibility differences (Schenck 1996) and the chemical shift artifact (Bernstein *et al* 2006). For a given patient, however, magnetic properties cannot be predicted and may not be constant in time. Therefore, patient-specific distortion characterization and/or correction has drawn considerable attention (Morgan *et al* 2004, Reinsberg *et al* 2005, Baldwin *et al* 2009, Crijns *et al* 2011, Wang *et al* 2013, Karaiskos *et al* 2014, Adjeiwaah *et al* 2018). The vast majority of these studies relied on either the field mapping technique (Jezzard and Balaban 1995) or the read gradient polarity reversal method (Chang and Fitzpatrick 1992), which both burden the imaging protocol with at least one extra sequence. Both methodologies not only account for susceptibility and chemical shift distortions but also for static magnetic field inhomogeneity related distortion (all three phenomena collectively referred to as sequence dependent distortions (Baldwin *et al* 2009)).

Within-patient tissue susceptibility effects have been widely investigated in simulation studies (Wachowicz *et al* 2010, Stanescu *et al* 2012, Lundman *et al* 2017). However, distortions at SRS and SRT target locations, including those induced by Gd-based contrast agents, have not been specifically studied. The paramagnetic nature of Gd alters the local magnetic field due to its magnetic susceptibility (molar susceptibility in SI units: 0.3393 ml mol^{-1} (Haacke and Reichenbach 2014)). Susceptibility difference inherently induces geometric distortion in and around a susceptibility cavity, with the spatial displacement of a given point varying according to the cavity location, size and orientation with respect to B_0 (Schenck 1996, Stanescu *et al* 2012, Brown *et al* 2014, Haacke and Reichenbach 2014).

In SRS treatment planning, inaccuracies in localization and margin delineation of brain lesions constitute a major cause of concern (Karaiskos *et al* 2014, Kirkpatrick *et al* 2015, Weygand *et al* 2016, Pappas *et al* 2017a). The need to define an optimal margin around the gross target volume (GTV) is of great importance in order to minimize radiation induced toxicity (Ma *et al* 2014), especially when multiple targets are treated such as in multiple brain metastases patients. A uniform margin of 1 mm has been reported to reduce the risk of normal brain radionecrosis compared to a 3 mm margin (Ma *et al* 2014, Kirkpatrick *et al* 2015). In other approaches, sub-millimeter or zero margins are routinely applied, minimizing the risk of radionecrosis (Ma *et al* 2014), but reducing or eliminating margins increases the risk of target underdosage and local recurrence. Geometric offsets of the order of 1 mm can result in considerable target underdosage, compromising treatment efficiency (Jursinic *et al* 2005, Karaiskos *et al* 2014, Seibert *et al* 2016, Pappas *et al* 2017a).

A previous study dealt with the characterization of system-related distortions arising from gradient field non-linearities in MR images employed in SRS applications (Pappas *et al* 2016). This study seeks to examine respective sequence dependent distortions. Emphasis is put on the geometric warping related to the magnetic susceptibility of the routinely administered Gd-DTPA contrast agent. To this purpose, a distortion detection phantom previously presented (Pappas *et al* 2016) was modified to incorporate inserts filled with Gd-DTPA at various concentrations. Distortion evaluation was performed using the read gradient polarity reversal methodology, in combination with the field mapping technique employed to assess and subtract background field variations. Furthermore, a similar methodology was applied to brain MR images in order to characterize and evaluate sequence dependent distortions at and in the vicinity of Gd-DTPA enhanced metastases. The effect of such distortions on SRS treatment planning and target definition is discussed.

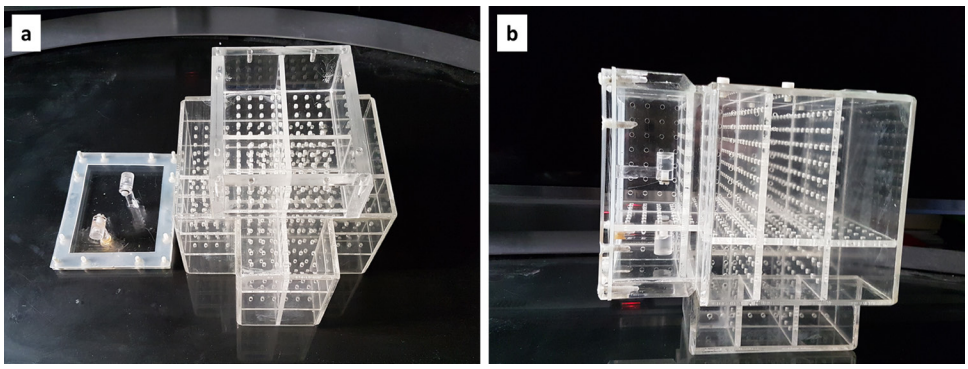

Figure 1. The distortion detection phantom used in this study. (a) Two cylindrical inserts were fixed on the removable top (superior side of the phantom) shown on the left. (b) The phantom positioned at scanning orientation with the top mounted on.

2. Materials and methods

2.1. Phantom study

2.1.1. Phantom description

An acrylic-based phantom, custom-made for distortion detection (Pappas *et al* 2016, 2017a), was utilized in this work. The head-sized phantom, that incorporates 947 control points (CPs) distributed over one sagittal, one coronal and three axial planes, was modified to accommodate two cylindrical inserts (inner dimensions of 8 mm diameter and 11 mm height, wall thickness of 1.8 mm) for the purposes of the present study (figure 1). The inserts were positioned at the superior side of the phantom with a 45 mm distance between them (figure 1(a)) and close to control points (figure 1(b)). Small plastic screws along with rubber flanges facilitated leakage proof filling with solutions, while acrylic posts ensured fixed position with respect to the removable top of the phantom (figure 1(a)). The installed cylindrical inserts, which can be regarded as two additional CPs, can be filled with a solution different from that of the phantom body, thus simulating two brain lesions within the brain parenchyma.

To investigate the magnitude of distortion induced by the paramagnetic contrast agent, the inserts were filled with varying concentrations of Gd-DTPA solution in saline. Both inserts were filled with saline (corresponding to zero concentration of Gd-DTPA), as well as with 5, 10 and 20 mM of Gd-DTPA diluted in saline. Although contrast agent concentration varies rapidly within the brain and especially within tumors and vessels, concentrations considered here are typical with respect to the ones encountered *in vivo* and cover the range of corresponding concentrations found in the literature (Weisskoff and Kiihne 1992, Fan *et al* 2007, De Rochefort *et al* 2008, Hijnen *et al* 2013). The phantom body was filled with standard copper sulfate solution (Gunter *et al* 2009, Pappas *et al* 2016) in order to achieve adequate signal intensity and high contrast with acrylic material.

2.1.2. MRI scanning

All phantom scans were performed at 1.5 T (Multiva, Philips Medical Systems, The Netherlands). The imaging protocol comprised of three-dimensional (3D), gradient recalled echo (GRE) pulse sequences with vendor-supplied distortion correction routines enabled. A phased array head coil was used for signal reception. Scanning sequences and parameters are summarized in table 1. In all image series, reconstructed pixel size was $0.98 \times 0.98\,\text{mm}^2$ with a slice thickness of 1 mm.

2.1.3. Read gradient polarity reversal technique

To evaluate the contrast agent induced distortion, the reversed read gradient polarity technique (Chang and Fitzpatrick 1992, Baldwin *et al* 2007, 2009, Moutsatsos *et al* 2013) was implemented. Briefly, this method relies on the fact that sequence dependent distortions (i.e. stemming from B_0 inhomogeneity, susceptibility differences and chemical shift artifacts (Baldwin *et al* 2009)) change sign with respect to frequency encoding direction. Therefore, the technique requires that the phantom is MR scanned twice using identical imaging parameters except for the read gradient polarity. The geometric offset between corresponding CPs identified in the two image series is twice the sequence dependent distortion magnitude (Moutsatsos *et al* 2013).

Acquired images from series #1–4 (table 1) were exported from the MR unit in dicom format and analyzed in MATLAB R2015b (The MathWorks, Inc., Natick, MA) using in-house routines. For every pair of image series (e.g. forward anterior–posterior (A–P) polarity and reversed posterior–anterior (P–A) polarity), the cylindrical inserts were identified in the 3D image stack by exploiting the signal void of the inserts' acrylic walls. By applying a simple thresholding procedure, binary images were obtained facilitating the estimation of the centroid (geometric center) of each insert within the dicom coordinate system. In addition, all CPs incorporated in the phantom

Table 1. MR scanning protocols and parameters used in the phantom study.

Image series #	MRI pulse sequence	Receiver bandwidth (Hz/pixel)	TE/TR/FA (ms/ms/°)	Read gradient axis and polarity	Acquisition time per 100 slices (min)	Gd-DTPA concentration in inserts (mM)
1	T1w spoiled GRE	191	4.6/25/30	*y*-axis/A-P	8.9	0, 5, 10, 20
2	T1w spoiled GRE	191	4.6/25/30	*y*-axis/P–A	8.9	0, 5, 10, 20
3	T1w spoiled GRE	191	4.6/25/30	*x*-axis/R–L	8.9	0, 5, 10, 20
4	T1w spoiled GRE	191	4.6/25/30	*x*-axis/L–R	8.9	0, 5, 10, 20
5	1st echo GRE	191	4.4/14/30	*y*-axis/A–P	5.0	0, 5, 10, 20
6	2nd echo GRE	191	6.8/14/30	*y*-axis/A–P	5.0	0, 5, 10, 20
7	1st echo GRE	191	4.4/14/30	*x*-axis/R–L	5.0	0, 5, 10, 20
8	2nd echo GRE	191	6.8/14/30	*x*-axis/R–L	5.0	0, 5, 10, 20

T1w: T1-weighted, GRE: gradient recalled echo, TE: echo time, TR: repetition time, FA: flip angle, A: anterior, P: posterior, L: left, R: right, Gd-DTPA: gadolinium diethylenetriamine pentaacetic acid.

were identified in both the forward and reversed MRI scans, using a localization algorithm described previously (Pappas *et al* 2016). Averaged (from the paired scans) CP or insert centroids were regarded as reference locations (assuming that polarity reversal results in the change of distortion sign without affecting the magnitude). Sequence dependent distortions (related to B_0 inhomogeneity and susceptibility effects) were estimated as the signed geometric offsets towards the polarity direction between reference locations (CP or insert centroids) and corresponding ones identified in the forward MRI scans. Residual sequence independent distortions (related to gradient field non-linearity (Baldwin *et al* 2009, Weygand *et al* 2016)), following the application of the vendor-supplied distortion correction, were not taken into account since they do not change sign with respect to read gradient polarity.

2.1.4. *Field mapping technique*

The well-established field mapping technique (Jezzard and Balaban 1995, Cusack *et al* 2003, Baldwin *et al* 2009, Jackson *et al* 2010, Wang *et al* 2013) was also implemented within the same MR imaging session. Briefly, the method requires the collection of two GRE pulse sequences, each with a different echo time (Brown *et al* 2014). Phase difference maps, $\Delta\varphi$, obtained through a time-consuming, phase unwrapping post-processing procedure (Cusack and Papadakis 2002), are directly proportional to magnetic field variations, ΔB, according to equation (1) (Baldwin *et al* 2009, Jackson *et al* 2010, Wang *et al* 2013):

$$\Delta B\,(x, y, z) = \frac{\Delta\varphi(x, y, z, \Delta TE)}{\gamma \Delta TE} \tag{1}$$

where $\Delta TE = TE2 - TE1$ is the echo time difference between the two echoes of the two sequences and γ is the proton gyromagnetic ratio. Magnetic field variations can be transformed to sequence dependent distortions on the frequency encoding axis, e.g. Δy if y-axis is the read gradient axis, using equation (2):

$$\Delta y(x, y, z) = \Delta B(x, y, z)/G_{fe} \tag{2}$$

where G_{fe} is the read gradient field strength on y-axis. Equations (1) and (2) define the distortion sign convention used.

To avoid severe phase wrapping, a ΔTE value of 2.40 ms was selected, at the expense of sensitivity. Imaging parameters used are summarized in table 1 (image series #5–8). The resulting wrapped phase difference maps were unwrapped by implementing the methodology described in the work of Cusack and Papadakis (2002), with the negated magnitude serving as the noise estimator field for guided unwrapping. In large areas of signal void, phase difference maps were dilated due to lack of phase information (Cusack *et al* 2003). However, phase difference maps at low signal areas were discarded and not used in the analysis. This post-processing step required several hours of computational time, although real-time image unwarping has also been proposed (Crijns *et al* 2011).

Unwrapped phase difference maps were used to determine sequence dependent distortion at the phantom CP locations within the 3D dicom coordinate system. Moreover, results were compared to the corresponding ones derived using the reversed read gradient polarity technique (see section 2.1.3) for validation purposes. Furthermore, the same methodology was followed to estimate B_0 inhomogeneity induced distortion exhibited in the vicinity of the cylindrical inserts filled with contrast agent solution.

2.1.5. Contrast agent induced offset

Net insert centroid offset stemming from Gd-DTPA susceptibility alone was deduced by subtracting the B_0 inhomogeneity related distortion at the respective insert region from the total distortion at the specific insert location as reflected by the total geometric offset of the insert centroid. The former was evaluated by the field mapping technique, whilst the latter was estimated as the signed geometric offset between reference insert centroid locations and corresponding ones identified in the forward MRI scans.

2.2. Patient study

Three patients referred to SRS for single or multiple brain metastases of variable sizes and locations were enrolled. All MR images were acquired at 1.5 T (Achieva, Philips Medical Systems, The Netherlands), following an intravenous Gd-DTPA injection of 0.2 mmol kg^{-1}. The institution's standard clinical protocol for Gamma Knife (Elekta Instruments AB, Stockholm, Sweden) SRS applications was implemented, which included the utilization of the Leksell stereotactic frame for patient immobilization and image registration purposes. The imaging protocol involved both the read gradient polarity reversal and field mapping techniques employing a set of pulse sequences similar to those used in the phantom study. Specific acquisition parameters were the same as the ones presented in table 1 for series #1, 2, 5 and 6 (only the y-axis was used as frequency encoding axis), apart from the receiver bandwidth which was set to 217 Hz/pixel. Acquisition times for 150 mm anatomical coverage with the T1w spoiled GRE sequence and the plain GRE sequence were 9.5 min and 5.3 min, respectively. The employed set of parameters reflects the one used clinically in our institution for SRS treatment planning purposes. The selected bandwidth level provides adequate signal-to-noise ratio (SNR) even for the tiniest brain lesions.

Patient images, reconstructed using a voxel size of $0.82 \times 0.82 \times 1.5\,mm^3$, were exported in dicom format and analyzed in MATLAB using in-house developed routines. A total of ten brain metastases were identified and contoured in both the forward and reverse read gradient polarity series using the automatic segmentation tool incorporated in the GammaPlan treatment planning system (ELEKTA, Sweden). Similar intensity threshold levels were employed in the two MR series resulting in identical target volumes. An experienced neurosurgeon (K.L.) reviewed all the obtained structures cross-checking the corresponding ones and either approved them or manually modified them in case the automatic tool had failed to accurately define the target volume. Contoured lesions were treated as CPs for distortion detection at the respective locations and, therefore, the followed approach was similar to that applied in the phantom study. Using the polarity reversal technique, the total sequence dependent distortion at a specific lesion location was calculated as half the geometric offset between the corresponding centroids in the dicom coordinate system. The field mapping technique was used to determine potential background field distortions in the vicinity of the identified lesions and, thus, to differentiate between contrast agent induced geometric offset and spatial degradation due to local B_0 inhomogeneities and chemical shift effects. Specifically, the mean distortion value within an unenhanced volume of interest close to a lesion was determined, and this value was subtracted from the total sequence dependent distortion estimated (using the polarity reversal method) for that lesion location to yield the net contrast agent induced offset.

3. Results

3.1. Phantom study

Table 2 summarizes the results on phantom CP distortions obtained with the read gradient polarity reversal technique and the field mapping method. Sequence dependent distortion magnitude greatly varies with respect to the distance from the MR scanner's isocenter and may exceed 1 mm. Mean detected distortion is of the order of 0.25 mm. Taking into account that the detected distortion for the CPs close to the isocenter is of the order of 0.1 mm, the observed sequence dependent distortions mainly stem from B_0 inhomogeneities and, thus, increase with distance from isocenter.

As a validation check for the developed image processing routines, detected distortions at CP locations derived using the field mapping method were compared with corresponding results obtained by employing the reversed read gradient polarity technique. Mean and median distortion differences were 0.03 mm and <0.01 mm, respectively. However, 14% of the CPs exhibited absolute distortion differences of >0.3 mm, with a maximum difference of 0.54 mm. Inspection of these specific CPs revealed that they lie at the lower limit of the field being imaged which corresponds to the inferior part of the sizeable phantom placed at the edge of the receiver head coil. These local discrepancies, therefore, are attributed to the compromised sensitivity of the receiver coil at its furthest part, resulting in reduced SNR and, potentially, phase shifts.

Regarding the cylindrical inserts filled with various concentrations of contrast agent, figure 2 demonstrates relevant distortion maps derived from the field mapping technique, as well as acquired T1w axial images, for the read gradient direction in the y-axis. Distortion maps (figures 2(a) and (d)) are presented for an axial slice lying centrally to the cylindrical inserts. Inserts with no contrast agent do not disturb the local magnetic field (figure 2(a)),

Table 2. Sequence dependent distortion magnitudes determined with the two employed methods by considering all 947 phantom control points. Axes refer to the dicom coordinate system. Decimal places provided signify numerical variation and not precision.

	Read gradient axis and polarity	Mean ± 1 std (mm)	Median (mm)	Max (mm)
Read gradient polarity reversal	*y*-axis/A–P	0.21 ± 0.22	0.14	1.22
	x-axis/L–R	0.30 ± 0.22	0.25	1.17
Field mapping	*y*-axis/A–P	0.21 ± 0.16	0.19	1.05
	x-axis/L–R	0.27 ± 0.16	0.24	1.12

A: anterior, P: posterior, L: left, R: right.

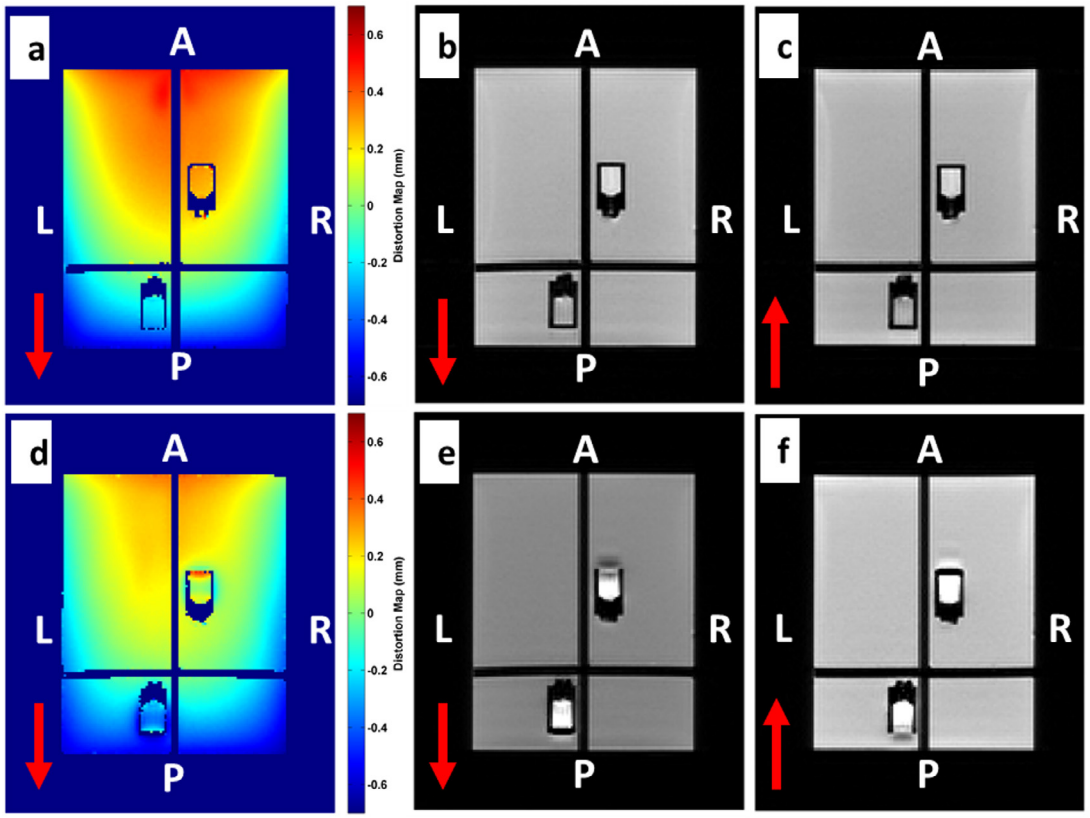

Figure 2. Axial slice intersecting the cylindrical inserts of the phantom with frequency encoding polarity direction set on anterior–posterior (a), (b), (d) and (e) or posterior–anterior (c) and (f). Inserts are filled with saline (no contrast agent) (top row) or 20 mM of Gd-DTPA (bottom row). (a) and (d) Distortion maps derived using the field mapping technique. (b), (c), (e) and (f) T1w images of the same slice. Red arrows depict polarity direction (L: left, R: right, A: anterior, P: posterior). Reversing read gradient polarity has no apparent effect on insert position but evidently displaces the contrast agent signal.

while for the maximum concentration considered a steep distortion gradient is identified at the insert borders (figure 2(d)). More specifically, the susceptibility related distortion gradient reaches its maximum values at the superior and inferior insert borders (not shown here). It should be noted that B_0 inhomogeneity related distortion was not constant and slightly varied between different scanning sessions, as evidenced by comparing figures 2(a) with (d), depending on phantom positioning with respect to the MR isocenter and auto-shimming procedures potentially performed.

As shown in figures 2(b) and (c), reversing the polarity of the read gradient direction does not evidently induce spatial offset of the inserts centroids in the case of no contrast agent presence. Contrarily, in the presence of the paramagnetic agent, inserts get mispositioned and, as demonstrated for the maximum concentration considered herein (figures 2(e) and (f)), specific insert walls appear severely distorted. The images acquired with the read gradient direction in the *x*-axis exhibited an analogous behavior with leftwards or rightwards geometric offsets depending on the selected polarity.

Figure 3(a) presents the estimated net centroid offsets (i.e. owing to the Gd-DTPA contrast agent) for the cylindrical inserts for the MR scans with frequency encoding set on the *y*-axis. As expected, net centroid offset varies considerably with Gd-DTPA concentration. Relatively lower net centroid offsets were detected (up to 1 mm for the 20 mM concentration) with the frequency encoding direction on *x*-axis (figure 3(b)), suggesting a weaker correlation between centroid mispositioning and contrast agent concentration for this setup.

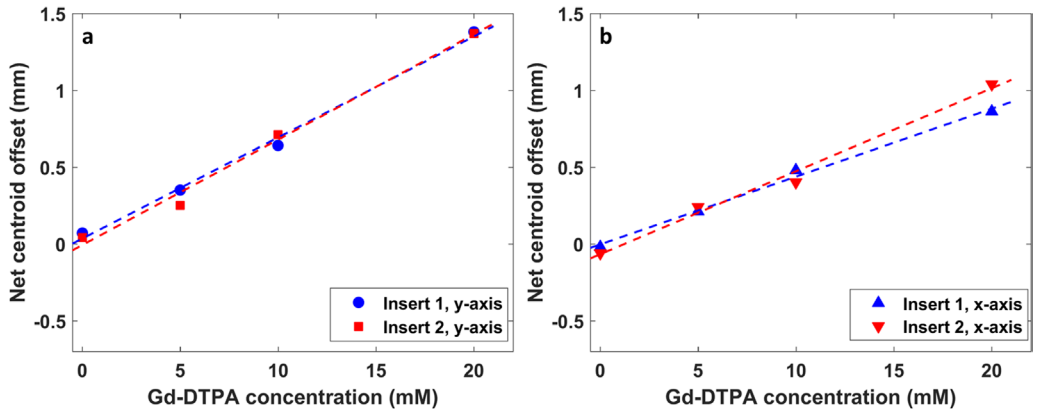

Figure 3. Estimated net centroid offset for both cylindrical inserts as a function of contrast agent concentration. (a) Frequency encoding direction set on the *y*-axis (P–A and A–P) of the dicom coordinate system. (b) Frequency encoding direction set on the *x*-axis (L–R and R–L) of the dicom coordinate system. Dashed lines were derived by linear fitting of the corresponding data.

A first order polynomial fit was applied to all datasets to determine the centroid offset, D, induced per unit of contrast agent concentration, C, i.e. $\left|\frac{\partial D}{\partial C}\right|$, as reflected by the slopes of the curves shown in figures 3(a) and (b). Obtained results are depicted in figure 4. Evidently, lower slopes were calculated for *x*-axis read gradient compared to *y*-axis read gradient.

3.2. Patient study

Table 3 summarizes the results of the patient study conducted. For each lesion, the total centroid offset identified in every axis using the reversed read gradient polarity is given. This offset corresponds to the overall target localization uncertainty due to patient-induced geometric distortion in MR images. In phase encoding directions, i.e. *x* and *z* axes, maximum centroid offset hardly exceeds 0.1 mm and represents the uncertainty of the experimental methodology adopted. In the frequency encoding direction (*y*-axis), total centroid offset magnitude is on average 0.54 mm and exceeds 0.75 mm in two cases (2.24 and 3.11 ppm, respectively). It should be noted that these results represent the distance between reference lesion centroid locations and corresponding ones identified in the forward polarity MR scan. Using the field mapping technique, distortion in the range of −0.12 up to 0.27 mm (table 3) was detected in regions of interest close to the targets but with no Gd-DTPA enhancement, mainly due to local B_0 magnetic field inhomogeneities. The directionality of this distortion either opposes or is the same with that of the susceptibility induced distortion, thus decreasing or increasing, respectively, the total uncertainty in target localization. Subtracting field mapping obtained distortion from the centroid offset in *y*-axis yields the net offset (i.e. centroid offset without effects from background field variations), which represents the Gd-DTPA susceptibility induced distortion. As presented in table 3, the net offset ranges between 0.43 and 0.65 mm (1.78 and 2.68 ppm, respectively), with an average value of 0.51 mm (2.11 ppm).

Figure 5(a) presents the distortion field, as estimated by the field mapping technique, of an axial image depicting metastases #4 and #5 (table 3). Figure 5(b) demonstrates the fusion of corresponding T1w images acquired with forward and reversed read gradient polarity. Matching pixels that exhibit different signal intensity in the two images are highlighted in color. Offsets between corresponding lesions in the two MR images are evident. A normalized signal intensity profile is given in figure 5(c), quantifying the detected offset along a line passing through the two metastases. Field mapping results suggest a background field distortion of the order of −0.10 mm at this area (figure 5(a) and table 3). Since the total centroid offset detected in the *y*-axis for the two metastases is slightly above +0.35 mm (table 3), it is deduced that the Gd-DTPA induced centroid offset approaches +0.5 mm. Contrarily, for metastasis #10 (table 3), the background distortion in the vicinity of the lesion was found equal to +0.24 mm (figure 6(a) and table 3). As a result, this distortion adds up to the estimated susceptibility induced offset (+0.63 mm, table 3) resulting in a total centroid offset of +0.87 mm (table 3 and figure 6(b)). Therefore, the spatial offset between the signal intensity profiles shown in figure 6(c) has been approximately doubled compared to the corresponding one shown in figure 5(c).

4. Discussion

Several studies have performed patient specific, sequence dependent distortion assessment in intracranial MR images, relying mainly on simulations or the field mapping technique. Specifically, Stanescu *et al* (2012) calculated geometric distortion stemming from susceptibility differences by assigning bulk susceptibility values in CT images of various anatomical sites, including the brain. Maximum calculated distortion reached 5.6 ppm

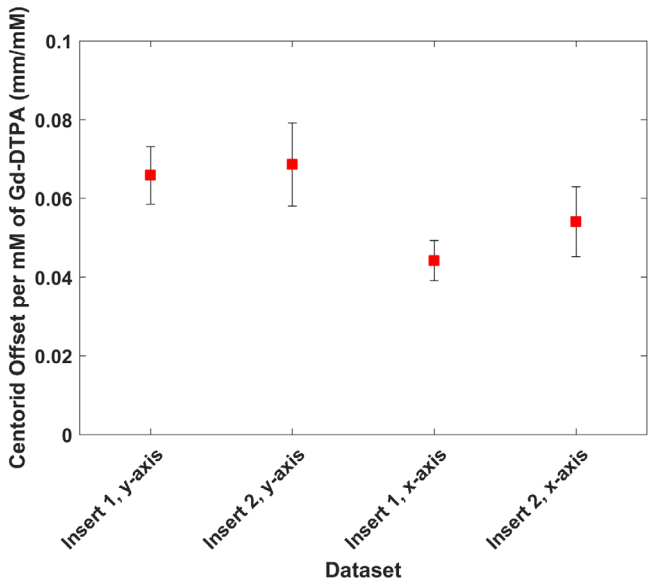

Figure 4. Fitted slopes for net centroid offset versus Gd-DTPA concentration. Error bars correspond to the uncertainty of the slopes (at 67% confidence level) as determined by linear regression analysis.

Table 3. Patient study results. For each metastasis, the total centroid offset provided by the reversed polarity technique is presented, along with the distortion detected using the field mapping technique. Net centroid offset in *y*-axis is deduced by subtracting the detected background distortion form the total centroid offset in *y*-axis. Axes refer to the dicom coordinate system. Decimal places provided signify numerical variation and not precision.

		Lesion characteristics			Total centroid offset (reversed polarity)			Distortion close to lesion (Field mapping)	Net centroid offset (mainly related to Gd-DTPA)	
Patient #	Met #	Volume (mm^3)	Distance from MR isocenter (mm)	Location on *z*-axis (mm)	*x*-axis (mm)	*y*-axis (mm)	*z*-axis (mm)	*y*-axis (mm)	*y*-axis (mm)	*y*-axis (ppm)
1	1	1107	67.8	33.4	−0.04	0.80	0.07	0.27	0.53	2.19
2	2	471	69.0	6.3	0.00	0.52	−0.03	−0.12	0.65	2.68
	3	48.4	20.6	−5.7	0.01	0.47	0.00	0.01	0.46	1.92
3	4	33.3	31.1	5.3	−0.02	0.35	−0.08	−0.12	0.47	1.96
	5	18.2	35.0	5.3	−0.02	0.38	0.10	−0.10	0.49	2.02
	6	52.4	54.2	17.3	−0.07	0.38	0.01	−0.06	0.44	1.82
	7	20.2	49.5	38.3	−0.04	0.51	0.08	0.08	0.43	1.78
	8	20.2	83.7	48.8	0.04	0.72	0.08	0.20	0.52	2.14
	9	272	362.2	50.3	0.06	0.37	−0.12	−0.10	0.47	1.95
	10	212	541.8	66.0	−0.07	0.87	−0.09	0.24	0.63	2.61

at air cavities. Wachowicz *et al* (2010) calculated susceptibility induced distortion in the brain in a rotating magnet, MR-linac design and reported maximum distortion of 7.1 ppm. Implementation of the field mapping technique in 19 intracranial MR scans by Wang *et al* (2013) revealed less than 4.4 ppm distortion near or around the sagittal sinuses. Although the above studies effectively detected or calculated patient dependent intracranial distortion, assessment of MR related, geometric uncertainty in brain lesion localization was not addressed. This study focused on the characterization and evaluation of sequence dependent distortion in and around brain lesions (i.e. the high dose areas) prescribed in contrast-enhanced MR images. A dedicated phantom and a limited number of patients, as well as pulse sequences and imaging parameters used clinically for SRS treatment planning, were employed to approximate real conditions.

In the phantom study of this work, both the read gradient polarity reversal and field mapping techniques were applied for sequence dependent distortion detection. Using the CPs of the phantom, results of both techniques were inter-compared for cross-validation. Results were found in excellent agreement, apart from CPs located at the far end of the receiver head coil and, thus, are well outside the treatable volume in brain SRS applications. As evidenced by data in figures 2(a) and (d), the field mapping technique is robust even in the presence of miniature distortions (e.g. 0.1 mm). However, the phase unwrapping step is time-consuming and may be subject

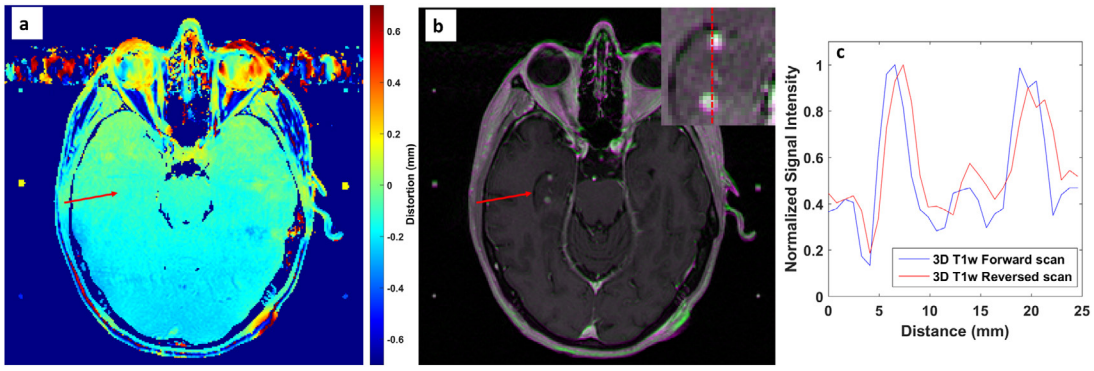

Figure 5. (a) Field mapping derived distortion map corresponding to an axial slice with two brain metastases (mets #4 and #5 in table 3). (b) Fused forward (A–P) and reversed (P–A) polarity MR images acquired using the clinically employed MR protocol for SRS treatment planning. Corresponding pixels with different values are depicted in color (green and purple for higher values in forward and reversed images, respectively). The area of the two metastases is depicted magnified in the insert. The red arrow points to the area of the two metastases. (c) Normalized pixel intensity profiles for the two images along the red dashed line that runs parallel to the *y*-axis of the dicom coordinate system.

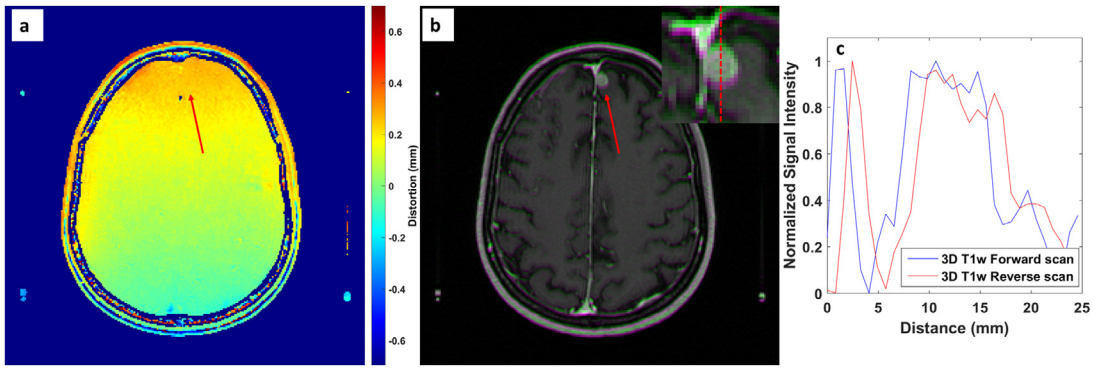

Figure 6. (a) Field mapping derived distortion map corresponding to an axial slice with one brain metastasis (met #10 in table 3). (b) Fused forward (A–P) and reversed (P–A) polarity MR images acquired using the clinically employed MR protocol for SRS treatment planning. Corresponding pixels with different values are depicted in color (green and purple for higher values in forward and reversed images, respectively). The metastasis area is depicted magnified in the insert. The red arrow points to the metastasis location. (c) Normalized pixel intensity profiles for the two images along the red dashed line that runs parallel to the *y*-axis of the dicom coordinate system.

to unwrapping errors (Cusack and Papadakis 2002, Cusack *et al* 2003). On the other hand, the read gradient polarity reversal method requires accurate boundary definition, since it is merely based on the subtraction of measurable offsets. Brain lesions were simulated as small cylindrical inserts lying in the periphery of the phantom. The inserts were filled with Gd-DTPA solution of varying concentration to study the contrast agent induced susceptibility effect. Using the field mapping technique, distortion values were found to vary considerably inside and close to the susceptibility cavity. Since it is unclear how these distortions translate to geometric offset, this technique was not used to evaluate contrast agent induced displacement. However, it was used to evaluate B_0 inhomogeneity related distortion close to the inserts in order to derive, employing results obtained with the read gradient polarity reversal method, the net centroid offset owing to the Gd-DTPA contrast agent.

Contrast agent presence was found to considerably affect phantom insert centroids, since mean values of 0.067 mm mM^{-1} and 0.054 mm mM^{-1} (corresponding to 0.205 ppm mM^{-1} and 0.165 ppm mM^{-1}, respectively) were estimated for read gradient direction in *x*-axis and *y*-axis, respectively. This difference could be attributed to the cylindrical shape of the inserts (Schenck 1996, Brown *et al* 2014, Haacke and Reichenbach 2014). Distortion magnitude in and around a susceptibility cavity is not constant and is expected to be maximized at the cavity borders (Schenck 1996, Haacke and Reichenbach 2014). In addition, it greatly depends on cavity size, shape and orientation with respect to B_0, as well as on imaging parameters used (Wachowicz *et al* 2010, Stanescu *et al* 2012, Brown *et al* 2014, Haacke and Reichenbach 2014). Therefore, quantitative results provided should only be treated as indicative for the specific MR imaging sequence and scanning parameters (which are, however, clinically used in SRS treatment planning) and a cylindrical cavity with a size of the order of 700 mm^3. In another phantom study (Hijnen *et al* 2013), the authors measured a Gd-induced distortion of 0.109 ppm mM^{-1} for an infinitely long cylinder parallel to B_0. Based on theoretical calculations for a spherical cavity, an offset of 0.218 ppm mM^{-1}

is expected at the cavity border and no frequency shift at the center (Hijnen *et al* 2013). Also, it should be pointed out that higher concentrations do not necessarily result in greater overall sequence dependent distortion magnitudes (i.e. including B_0 inhomogeneity) at the insert locations. This is because the two distortion vector components, stemming from susceptibility differences due to the presence of the Gd-DTPA contrast agent and from B_0 inhomogeneity, respectively, may point to different directions.

In the patient study of this work, effort was made to characterize the distortion at brain metastases locations. A methodology similar to that used in the phantom study was implemented to dissociate distortion stemming from B_0 inhomogeneity and potential chemical shift effects from susceptibility induced distortion. B_0 inhomogeneity related distortion opposed susceptibility related offset at inferior brain areas, resulting in minimal overall centroid offsets. At superior brain areas, however, B_0 inhomogeneity changed sign, increasing considerably the total distortion as reflected by overall centroid offset. Maximum detected overall centroid offset approached 0.9 mm (3.73 ppm) for the specific set of brain lesion locations examined and imaging parameters used. It should be noted that metastases lying in even more distant areas from MR isocenter are expected to exhibit even higher distortion magnitude due to further B_0 homogeneity degradation (Baldwin *et al* 2009). Since sequence dependent distortion scales linearly with B_0 (Weygand *et al* 2016), an almost double offset would be realized at 3.0 T. Other sources of MR-related geometric degradation in SRS applications include gradient non-linearity and the stereotactic frame used for patient immobilization and image registration. For the lesion locations considered herein, gradient non-linearity induced distortion, exhibited on any axis, can reach 0.8 mm (Pappas *et al* 2016).

Several caveats of the current study are noteworthy. Presented results are only valid for the specific scanner, magnetic field strength, acquisition parameters (e.g. echo time), contrast agent concentrations, target sizes, shapes and orientations with respect to B_0 assumed in this study. A comprehensive study regarding the contradictory effects of receiver bandwidth on distortion magnitude and SNR was not performed. The auto-shimming process could have been disabled or shimming conditions could have been manually imported to ensure identical B_0 inhomogeneity circumstances among the various MR scanning sessions of the phantom study. Moreover, *in vivo* contrast agent concentration varies with administration dosage and time (Fan *et al* 2007, De Rochefort *et al* 2008, Lind *et al* 2017). Therefore, quantitative results should be treated as indicative for the experimental conditions used herein. In patient studies, the extra imaging time required constitutes a major limitation of the proposed methodology. The uncertainty related to the brain lesion contouring process was not evaluated, although effort was put to minimize the variability in target definition between the forward and reversed read gradient polarity MR series. Moreover, sequence dependent distortion in areas away from targets (i.e. at low dose areas) was not evaluated, although it is expected to reach several millimeters at tissue-air interfaces (Stanescu *et al* 2012, Wang *et al* 2013). This remark also suggests that in certain clinical cases, such as acoustic neuromas where the target lies close to the bone-air interface, increased sequence dependent distortion could be exhibited. Residual sequence independent distortions were not considered, whilst no attempt was made to correct for detected distortions. The clinical significance of the presented results was not assessed. A patient study of adequate sample size which will comprise of various clinical cases is warranted to assess the true clinical impact of sequence dependent distortions. Future work should also focus on the implementation and comparison of MR image correction schemes.

For the MRI protocol and imaging conditions used in this study, as well as the set of metastases locations examined, an average sequence dependent distortion of 0.54 mm (2.24 ppm) was estimated. Although this distortion magnitude may be regarded as relatively small, compared to the MR distortion or spatial uncertainty emanating from other sources, its effect on target localization in SRS treatment planning can be easily appreciated by simply acquiring an extra MR image series with reversed read gradient polarity. During target definition and treatment planning, both the forward and reversed polarity series, which are *a priori* spatially co-registered provided that the patient did not move, can be taken into account. The target contour or applied margins can be extended to cover the target identified in both image series. Another approach would be to correct acquired images for sequence dependent distortion and use the corrected series for target localization. To this purpose, several methods have been proposed (Chang and Fitzpatrick 1992, Morgan *et al* 2004, Reinsberg *et al* 2005, Karaiskos *et al* 2014, Pappas *et al* 2017b). However, implementation of these methods in routine clinical practice is not straightforward, while it requires painstaking image processing steps which need to be validated.

5. Conclusion

Target mispositioning due to MRI distortion could adversely affect the efficiency of SRS planning, especially in locations where Gd-DTPA induced susceptibility and B_0 inhomogeneity add up to each other, thus resulting in increased overall distortion. The field mapping technique is suitable to provide sequence dependent distortion maps, but the reversed read gradient polarity method allows for a more straightforward and efficient visualization of the sequence dependent distortion at target locations. By carefully inspecting both the forward and reversed

polarity image series during treatment planning and target/margin definition, sequence dependent distortion can be easily taken into consideration and partially dealt with.

ORCID iDs

Eleftherios P Pappas https://orcid.org/0000-0003-4030-2241

References

Adjeiwaah M, Bylund M, Lundman J A, Thellenberg Karlsson C, Jonsson J H and Nyholm T 2018 Quantifying the effect of 3T MRI residual system and patient-induced susceptibility distortions on radiotherapy treatment planning for prostate cancer *Int. J. Radiat. Oncol.* **100** 317–24

Baldwin L L N, Wachowicz K and Fallone B G 2009 A two-step scheme for distortion rectification of magnetic resonance images *Med. Phys.* **36** 3917

Baldwin L L N, Wachowicz K, Thomas S D S, Rivest R and Fallone B G 2007 Characterization, prediction, and correction of geometric distortion in 3 T MR images *Med. Phys.* **34** 388

Bernstein M A, Huston J and Ward H A 2006 Imaging artifacts at 3.0T *J. Magn. Reson. Imaging* **24** 735–46

Brown R W, Cheng Y-C N, Haacke E M, Thompson M R and Venkatesan R 2014 *Magnetic Resonance Imaging: Physical Properties and Sequence Design* (New York: Wiley) (https://doi.org/10.1002/9781118633953)

Chang H and Fitzpatrick J M 1992 A technique for accurate magnetic resonance imaging in the presence of field inhomogeneities *IEEE Trans. Med. Imaging* **11** 319–29

Crijns S P M, Raaymakers B W and Lagendijk J J W 2011 Real-time correction of magnetic field inhomogeneity-induced image distortions for MRI-guided conventional and proton radiotherapy *Phys. Med. Biol.* **56** 289–97

Cusack R and Papadakis N 2002 New robust 3-D phase unwrapping algorithms: application to magnetic field mapping and undistorting echoplanar images *Neuroimage* **16** 754–64

Cusack R, Brett M and Osswald K 2003 An evaluation of the use of magnetic field maps to undistort echo-planar images *Neuroimage* **18** 127–42

Damyanovich A Z, Rieker M, Zhang B, Bissonnette J-P and Jaffray D A 2018 Design and implementation of a 3D-MR/CT geometric image distortion phantom/analysis system for stereotactic radiosurgery *Phys. Med. Biol.* **63** 075010

De Rochefort L, Nguyen T, Brown R, Spincemaille P, Choi G, Weinsaft J, Prince M R and Wang Y 2008 *In vivo* quantification of contrast agent concentration using the induced magnetic field for time-resolved arterial input function measurement with MRI *Med. Phys.* **35** 5328–39

Doran S J, Charles-Edwards L, Reinsberg S A and Leach M O 2005 A complete distortion correction for MR images: I. Gradient warp correction *Phys. Med. Biol.* **50** 1343–61

Fan X, Medved M, Karczmar G S, Yang C, Foxley S, Arkani S, Recant W, Zamora M A, Abe H and Newstead G M 2007 Diagnosis of suspicious breast lesions using an empirical mathematical model for dynamic contrast-enhanced MRI *Magn. Reson. Imaging* **25** 593–603

Gunter J L, Bernstein M A, Borowski B J, Ward C P, Britson P J, Felmlee J P, Schuff N, Weiner M and Jack C R 2009 Measurement of MRI scanner performance with the ADNI phantom *Med. Phys.* **36** 2193–205

Gustafsson C, Nordström F, Persson E, Brynolfsson J and Olsson L E 2017 Assessment of dosimetric impact of system specific geometric distortion in an MRI only based radiotherapy workflow for prostate *Phys. Med. Biol.* **62** 2976–89

Haacke E M and Reichenbach J R 2014 *Susceptibility Weighted Imaging in MRI: Basic Concepts and Clinical Applications* (Hoboken, NJ: Wiley-Blackwell) (https://doi.org/10.1002/9780470905203)

Hijnen N M, Elevelt A, Pikkemaat J, Bos C, Bartels L W and Grüll H 2013 The magnetic susceptibility effect of gadolinium-based contrast agents on PRFS-based MR thermometry during thermal interventions *J. Ther. Ultrasound* **1** 8

Jackson E F, Bronskill M J, Drost D J, Och J, Sobol W T and Clarke G D 2010 Acceptance testing and quality assurance procedures for magnetic resonance imaging facilities report of mr subcommittee task group I *AAPM Report* No. *100* (American Association of Physicists in Medicine)

Jezzard P and Balaban R S 1995 Correction for geometric distortion in echo planar images from B_0 field variations *Magn. Reson. Med.* **34** 65–73

Jin H, Keeling V P, Ali I and Ahmad S 2016 Dosimetric effects of positioning shifts using 6D-frameless stereotactic Brainlab system in hypofractionated intracranial radiotherapy *J. Appl. Clin. Med. Phys.* **17** 5682

Johnstone E, Wyatt J J, Henry A M, Short S C, Sebag-Montefiore D, Murray L, Kelly C G, McCallum H M and Speight R 2017 A systematic review of synthetic CT generation methodologies for use in MRI-only radiotherapy *Int. J. Radiat. Oncol.* **100** 199–217

Jursinic P A, Rickert K, Gennarelli T A and Schultz C J 2005 Effect of image uncertainty on the dosimetry of trigeminal neuralgia irradiation *Int. J. Radiat. Oncol. Biol. Phys.* **62** 1559–67

Karaiskos P, Moutsatsos A, Pappas E, Georgiou E, Roussakis A, Torrens M and Seimenis I 2014 A simple and efficient methodology to improve geometric accuracy in gamma knife radiation surgery: implementation in multiple brain metastases *Int. J. Radiat. Oncol. Biol. Phys.* **90** 1234–41

Karger C P, Höss A, Bendl R, Canda V and Schad L 2006 Accuracy of device-specific 2D and 3D image distortion correction algorithms for magnetic resonance imaging of the head provided by a manufacturer *Phys. Med. Biol.* **51** N253–61

Kirkpatrick J P *et al* 2015 Defining the optimal planning target volume in image-guided stereotactic radiosurgery of brain metastases: results of a randomized trial *Int. J. Radiat. Oncol. Biol. Phys.* **91** 100–8

Lind E, Knutsson L, Kämpe R, Ståhlberg F and Wirestam R 2017 Assessment of MRI contrast agent concentration by quantitative susceptibility mapping (QSM): application to estimation of cerebral blood volume during steady state *Magn. Reson. Mater. Phys. Biol. Med.* **30** 555–66

Lundman J A, Bylund M, Garpebring A, Thellenberg Karlsson C and Nyholm T 2017 Patient-induced susceptibility effects simulation in magnetic resonance imaging *Phys. Imaging Radiat. Oncol.* **1** 41–5

Ma L, Sahgal A, Larson D A, Pinnaduwage D, Fogh S, Barani I, Nakamura J, McDermott M and Sneed P 2014 Impact of millimeter-level margins on peripheral normal brain sparing for gamma knife radiosurgery *Int. J. Radiat. Oncol. Biol. Phys.* **89** 206–13

McRobbie D W, Moore E A and Graves M J 2017 *MRI from Picture to Proton.* (Cambridge: Cambridge University Press)

Morgan P S, Bowtell R W, McIntyre D J O and Worthington B S 2004 Correction of spatial distortion in EPI due to inhomogeneous static magnetic fields using the reversed gradient method *J. Magn. Reson. Imaging* **19** 499–507
Moutsatsos A, Karaiskos P, Petrokokkinos L, Sakelliou L, Pantelis E, Georgiou E, Torrens M and Seimenis I 2013 Assessment and characterization of the total geometric uncertainty in Gamma Knife radiosurgery using polymer gels *Med. Phys.* **40** 031704
Owrangi A M, Greer P B and Glide-Hurst C K 2018 MRI-only treatment planning: benefits and challenges *Phys. Med. Biol.* **63** 05TR01
Pappas E P, Alshanqity M, Moutsatsos A, Lababidi H, Alsafi K, Georgiou K, Karaiskos P and Georgiou E 2017a MRI-related geometric distortions in stereotactic radiotherapy treatment planning: evaluation and dosimetric impact *Technol. Cancer Res. Treat.* **16** 1120–9
Pappas E P, Dellios D, Seimenis I, Moutsatsos A, Georgiou E and Karaiskos P 2017b Review and comparison of geometric distortion correction schemes in MR images used in stereotactic radiosurgery applications *J. Phys.: Conf. Ser.* **931** 012031
Pappas E P, Seimenis I, Moutsatsos A, Georgiou E, Nomikos P and Karaiskos P 2016 Characterization of system-related geometric distortions in MR images employed in Gamma Knife radiosurgery applications *Phys. Med. Biol.* **61** 6993–7011
Reinsberg S A, Doran S J, Charles-Edwards E M and Leach M O 2005 A complete distortion correction for MR images: II. Rectification of static-field inhomogeneities by similarity-based profile mapping *Phys. Med. Biol.* **50** 2651–61
Roper J, Chanyavanich V, Betzel G, Switchenko J and Dhabaan A 2015 Single-isocenter multiple-target stereotactic radiosurgery: risk of compromised coverage *Int. J. Radiat. Oncol. Biol. Phys.* **93** 540–6
Schenck J F 1996 The role of magnetic susceptibility in magnetic resonance imaging: MRI magnetic compatibility of the first and second kinds *Med. Phys.* **23** 815
Schmidt M A and Payne G S 2015 Radiotherapy planning using MRI *Phys. Med. Biol.* **60** R323–61
Seibert T M *et al* 2016 Distortion inherent to magnetic resonance imaging can lead to geometric miss in radiosurgery planning *Pract. Radiat. Oncol.* **6** e319–28
Stanescu T, Wachowicz K and Jaffray D A 2012 Characterization of tissue magnetic susceptibility-induced distortions for MRIgRT *Med. Phys.* **39** 7185–93
Tadic T, Jaffray D A and Stanescu T 2014 Harmonic analysis for the characterization and correction of geometric distortion in MRI *Med. Phys.* **41** 112303
Wachowicz K, Stanescu T, Thomas S D and Fallone B G 2010 Implications of tissue magnetic susceptibility-related distortion on the rotating magnet in an MR-linac design *Med. Phys.* **37** 1714–21
Wang D, Strugnell W, Cowin G, Doddrell D M and Slaughter R 2004 Geometric distortion in clinical MRI systems: Part I: evaluation using a 3D phantom *Magn. Reson. Imaging* **22** 1211–21
Wang H, Balter J and Cao Y 2013 Patient-induced susceptibility effect on geometric distortion of clinical brain MRI for radiation treatment planning on a 3T scanner *Phys. Med. Biol.* **58** 465–77
Weisskoff R M and Kiihne S 1992 MRI susceptometry: image-based measurement of absolute susceptibility of MR contrast agents and human blood *Magn. Reson. Med.* **24** 375–83
Weygand J, Fuller C D, Ibbott G S, Mohamed A S R, Ding Y, Yang J, Hwang K P and Wang J 2016 Spatial precision in magnetic resonance imaging-guided radiation therapy: the role of geometric distortion *Int. J. Radiat. Oncol. Biol. Phys.* **95** 1304–16
Winey B and Bussiére M 2014 Geometric and dosimetric uncertainties in intracranial stereotatctic treatments for multiple nonisocentric lesions *J. Appl. Clin. Med. Phys.* **15** 122–32